AFRL-RX-WP-TP-2011-4303

CHARACTERIZATION OF HIGH CYCLE FATIGUE BEHAVIOR OF A NEW GENERATION ALUMINUM LITHIUM ALLOY (PREPRINT)

P.S. De and R.S. Mishra

**Missouri University of Science and Technology
(formerly Missouri University – Rolla)**

J.A. Baumann

The Boeing Company

JULY 2011

STINFO COPY

**AIR FORCE RESEARCH LABORATORY
MATERIALS AND MANUFACTURING DIRECTORATE
WRIGHT-PATTERSON AIR FORCE BASE, OH 45433-7750
AIR FORCE MATERIEL COMMAND
UNITED STATES AIR FORCE**

REPORT DOCUMENTATION PAGE

1. REPORT DATE *(DD-MM-YY)*
July 2011

2. REPORT TYPE
Journal Article Preprint

3. DATES COVERED *(From - To)*
01 July 2011 – 01 July 2011

4. TITLE AND SUBTITLE
CHARACTERIZATION OF HIGH CYCLE FATIGUE BEHAVIOR OF A NEW GENERATION ALUMINUM LITHIUM ALLOY (PREPRINT)

5a. CONTRACT NUMBER
FA8650-04-C-5704

5b. GRANT NUMBER

5c. PROGRAM ELEMENT NUMBER
62102F

6. AUTHOR(S)
P.S. De and R.S. Mishra (Missouri University of Science and Technology)
J.A. Baumann (The Boeing Company)

5d. PROJECT NUMBER
4347

5e. TASK NUMBER
00

5f. WORK UNIT NUMBER
25100000

7. PERFORMING ORGANIZATION NAME(S) AND ADDRESS(ES)
Missouri University of Science and Technology
(formerly Missouri University – Rolla)
1870 Miner Circle
Rolla, MO 65409

The Boeing Company
St. Louis, MO 63166

8. PERFORMING ORGANIZATION REPORT NUMBER

9. SPONSORING/MONITORING AGENCY NAME(S) AND ADDRESS(ES)
Air Force Research Laboratory
Materials and Manufacturing Directorate
Wright-Patterson Air Force Base, OH 45433-7750
Air Force Materiel Command
United States Air Force

10. SPONSORING/MONITORING AGENCY ACRONYM(S)
AFRL/RXLM

11. SPONSORING/MONITORING AGENCY REPORT NUMBER(S)
AFRL-RX-WP-TP-2011-4303

12. DISTRIBUTION/AVAILABILITY STATEMENT
Approved for public release; distribution unlimited.

13. SUPPLEMENTARY NOTES
PAO Case Number: 88ABW 2010-6748; Clearance Date: 03 Jan 2011. Document contains color.
Journal article submitted to *Acta Materialia*.

14. ABSTRACT
The high cycle fatigue life characteristics of an Al-Li alloy was studied as a function of microstructure. For the parent microstructure, fatigue life decreased with an increase in the grain size. No such effect was however noted at high stresses. This decrease in fatigue life was correlated with the lower crack initiation life arising due to small crack effect. Under multiaxial stress conditions, the alloy exhibited intergranular type of cracking. The cross-linking of intergranular cracks (in T8 condition) caused a further deterioration in fatigue life. Additionally, planar type of slip movements (in T3 condition) in stage-I crack propagation was observed. The slip planarity depended on both the sample texture and the nature of precipitates. Fractographic and textural evidences for this are presented.

15. SUBJECT TERMS
aluminum alloys, fatigue, fracture

16. SECURITY CLASSIFICATION OF:

a. REPORT	**b. ABSTRACT**	**c. THIS PAGE**
Unclassified	Unclassified	Unclassified

17. LIMITATION OF ABSTRACT:
SAR

18. NUMBER OF PAGES
38

19a. NAME OF RESPONSIBLE PERSON (Monitor)
Donna L. Ballard
19b. TELEPHONE NUMBER *(Include Area Code)*
N/A

CHARACTERIZATION OF HIGH CYCLE FATIGUE BEHAVIOR OF A NEW GENERATION ALUMINUM LITHIUM ALLOY

P.S.De, R.S. Mishra and J.A. Baumann*

Center for Friction Stir Processing, Department of Materials Science and Engineering

Missouri University of Science and Technology, Rolla, MO 65409

*The Boeing Company, St. Louis, MO 63166, USA

ABSTRACT

The high cycle fatigue life characteristics of an Al-Li alloy was studied as a function of microstructure. For the parent microstructure, fatigue life decreased with an increase in the grain size. No such effect was however noted at high stresses. This decrease in fatigue life was correlated with the lower crack initiation life arising due to small crack effect. Under multiaxial stress conditions, the alloy exhibited intergranular type of cracking. The cross-linking of intergranular cracks (in T8 condition) caused a further deterioration in fatigue life. Additionally, planar type of slip movements (in T3 condition) in stage-I crack propagation was observed. The slip planarity depended on both the sample texture and the nature of precipitates. Fractographic and textural evidences for this are presented.

Keywords: Aluminum alloys, Fatigue, Fracture

1.   INTRODUCTION

The aluminum-lithium alloys constitute a promising group of metallic material – with prospective applications in the aerospace industry. This is primarily due to its unique combination of low density and high strength. However, the microstructural complexity of these alloys with corresponding deleterious effects on mechanical properties has prevented its widespread use. Consequent research to improve mechanical properties has resulted in newer compositional modifications for this group of alloys. However, no detailed fatigue behavior evaluation for such new alloys exists in current literature. The present work therefore characterizes the high cycle fatigue and ductility behavior of a latest commercially available aluminum-lithium alloy. In the next subsection, a brief background of the precipitate type and its influence on deformation formed in different Al-Li alloys is provided.

1.1 Precipitates in Al-Li alloys

In Al-Li alloys, precipitation hardening (PH) constitutes the principal strengthening mechanism; therefore, the nature and type of precipitates is an area of prime interest. Considering the Al-Li phase diagram first, binary Al-Li alloys consists of grain boundary δ (AlLi) phase with coherent ordered δ' (Al_3Li) phase distributed within the matrix. Depending on the Li content, ternary Al-Cu-Li alloys are classified into two types. In the first type of alloy with low Li content, (e.g. Li - 1.15% and Cu - 5.15%), partially coherent θ' plates (transition phase of Al_2Cu), T_1 (Al_2CuLi) and T_B ($Al_{7.5}Cu_4Li$) are the principal strengthening phases [1]. For alloys with high Li (e.g. Cu - 2.7% and Li - 2.25%), θ', T_1 and coherent ordered δ' phases form. In ternary Al-Li-Mg system (e.g. Mg: 5.5%, Li 2%), incoherent Al_2LiMg and coherent δ' are the principal phases [1]. For Al-Li-Cu-Mg alloys, precipitation is similar to ternary Al-Cu-Li and is a function of its Cu:Li ratio. Thus, for low Cu:Li (<1.5) S' (Al_2CuMg), T_1 and ordered δ' are the principal precipitating phases [2, 3, 4]. At higher Cu:Li ratios (>2-3), precipitation is restricted to S' and T_1 phases only [2, 3, 4].

1.2 Effect of precipitates on slip and deformation characteristics

As already discussed, depending on the Al-Li composition, a wide variety of precipitating phases exist. This precipitate type variation significantly alters the dislocation slip mechanisms. Depending on slip band appearance or dislocation structure present (in transmission electron microscopy (TEM) experiments), slip in face centered cubic (f.c.c.) alloys is classified into two categories, a) wavy type and b) planar type. Thus for a wavy slip metal, slip bands exhibit a homogeneous structure. For planar slip situation a heterogeneous structure is observed [5]. The TEM observation of monotonically stretched wavy slip metal is characterized by dislocation bundles. A multipolar dislocation structure with extended dislocation pileups have been noted for planar slip metals [6]. Although, the exact reason behind such differences are not understood at present, short range ordering and clustering are thought to be a determining factor in this regard [6]. Variables like stacking fault energy and yield stress (controlling screw dislocation annihilation distance) were deemed to be of secondary importance [6].

Thus, binary Al-Li alloy with coherent ordered precipitates (δ') exhibits a planar slip tendency [7]. The grain boundary second phase and precipitate free zones (PFZ) contribute to additional strain localization [7]. Such slip heterogeneities have been associated with a low fatigue crack initiation resistance [7]. Similarly δ' and grain boundary second phases (θ', T_1, T_2, β') reduce the fracture toughness values in a Al-Li-Cu-Zr alloy [8]. Identically, δ' precipitates present in Al-Li-Cu-Mg-Zr alloy of the low Cu:Li type, resulted in strain localization during low cycle fatigue [9]. Thus, planar slip in Al-Li alloys is associated with coherent ordered δ' phase and results in an overall degradation in property. As an exception, Khireddine et al. [10] however envisaged that slip planarity induced crack bifurcation can result in improved fracture toughness values. Conversely, T/S phases present in Al-Li alloys promotes slip homogenization leading to a wavy slip characteristics resulting in an improvement in mechanical properties [9]. Here, it needs to be added that as observed in this study, texture plays a critical role in enhancing this slip planarity. The effect has been discussed in more detail later in this paper.

1.3 Effect of texture on deformation during fatigue

The first detailed examination of texture (predominantly {110}<112> and {100}<011> type) and grain size effect on the cyclic stress strain (CSS) life of Al-Li-Cu-Mg alloys was done by Khireddine et al. [10]. In the above mentioned work, samples extracted from the surface of an extruded bar showed a lower CSS life compared to those machined from the core. This CSS life change with sample location was attributed to an increased {111} pole density in the surface samples compared to those from within the core [10]. An additional decrease in CSS life with sample orientation change (from the longitudinal to a transverse direction of rolling) was also reported. The variation was attributed to a grain size effect [10]. Similar deformation texture effect on AA2090 alloy caused a reduced high cycle fatigue life at an orientation 45˚ to the rolling direction [9].

1.4 Multiaxial stresses in bending fatigue

Although practical loading conditions are multiaxial in nature, all cyclic deformation work on Al-Li alloys reported till date have been of the uniaxial type. Thus, understanding the effect of multiaxial stress states on Al-Li fatigue is of scientific and technological importance. Depending on the specimen used, multiaxial fatigue testing techniques are classified into two principal types, a) cruciform and b) thin walled tubular kind. Testing such standard multiaxial specimens is however associated with an elaborate equipment requirement. A simpler approach therefore would be to use a bending type fatigue specimen. The remaining part of this section discusses the nature of stresses in a displacement controlled fully reversed subsize bending fatigue sample of the type used in this work [11].

From the structural viewpoint, a displacement controlled fatigue specimen [11] behaves like a cantilever beam bent under point loading (Fig. 1), where b is the beam width at any section (ab = cd) and 'h' the thickness (ad = bc) which is uniform throughout the beam. The first order stress distribution for such conditions can be approximated as [12],

$$
\begin{aligned}
s_{11} &= -\frac{6Pxz}{bh^3} \\
s_{22} &= 0 \\
s_{13} &= -\frac{6P}{bh^3}\left(\frac{h^2}{4} - z^2\right)
\end{aligned}
\tag{1}
$$

The corresponding displacement relationships can be approximated as [12]

$$
\begin{aligned}
u &= \frac{Px^2z}{2EI} + \frac{vPz^3}{6EI} - \frac{Pz^3}{6IG} - \frac{Pl^2z}{2EI} + \frac{Ph^2z}{2IG} \\
w &= \frac{vPxz^2}{2EI} + \frac{Px^3}{6EI} - \frac{Pl^2x}{2EI} + \frac{Pl^3}{3EI}
\end{aligned}
\tag{2}
$$

where u is the x displacement and w is the z displacement, while E, G, v and I have their usual meanings. In the subsize bending fatigue test, w is the independent variable with load P and stress s_{11} is a function of displacement. Substituting, P in terms of w, x and z from Eq. (2) and for a constant x/b ratio (~2) the variation of s_{11} with sample thickness can be approximated as

Approved for public release; distribution unlimited.

$$s_{11} \approx \frac{3zwE}{3vz^2 + x^2 + l^2(l/b - 3)} \tag{3}$$

Thus, for a given w, s_{11} decreases with increasing sample thickness.

As already indicated, for the bending fatigue sample, tensile/compressive stress is highest at the sample surface and is zero at mid-section (i.e. neutral plane). The shear stress (s_{13}) on the other hand is highest at the midsection, and zero at the surface region. The exact stress distribution will however vary significantly, depending upon the nature of load and sample dimensions used. A more accurate measure of the expected stress variation can be obtained by using the appropriate boundary conditions and sample dimensions in a finite element analysis (FEA). In Fig. 1(b) and 1(c) the stress distribution across thickness at different positions in the subsize fatigue specimen as obtained using FEA is presented. The simulation was conducted for elastic conditions using ABAQUS software. The three dimensional specimen was meshed using 10 node tetrahedral elements with quadratic interpolation to predict function values at positions intermediate between nodes. The results show that stress condition along the specimen centerline is similar to that of pure bending with s_{11} as the measured stress. On the other hand, towards the specimen edge other than s_{11} and s_{13} an additional s_{12} component was predicted. Thus, in terms of principal stresses the stress state at specimen centre is uniaxial while towards the edges it is of the plane stress type. This stress state simulation was done assuming continuum conditions. However, grain boundary phases present will lead to discontinuities affecting the overall stress state. Thus, plane stress conditions at such discontinuities, initiates triaxial stress states. This background discussion will become important for later parts of this paper as de-lamination is a typical feature observed in aged Al-Li alloys [9]. In laminated structures, depending on the arrangement of laminates three different classifications are possible. They are, (a) crack arrester, (b) crack divider and (c) short transverse type respectively [12-13]. This can significantly affect the fatigue life as will be discussed in the later part of this work.

In the preceding sections the sensitivity of fatigue property on the microstructural characteristics of Al-Li alloys was highlighted. Newer manufacturing processes like friction stir welding/processing have introduced further complexities into this structure-property relationship. The current work explores the

microstructural and stress state effects on the high cycle fatigue life of a latest generation Al-Li alloy and its friction stir processed variant.
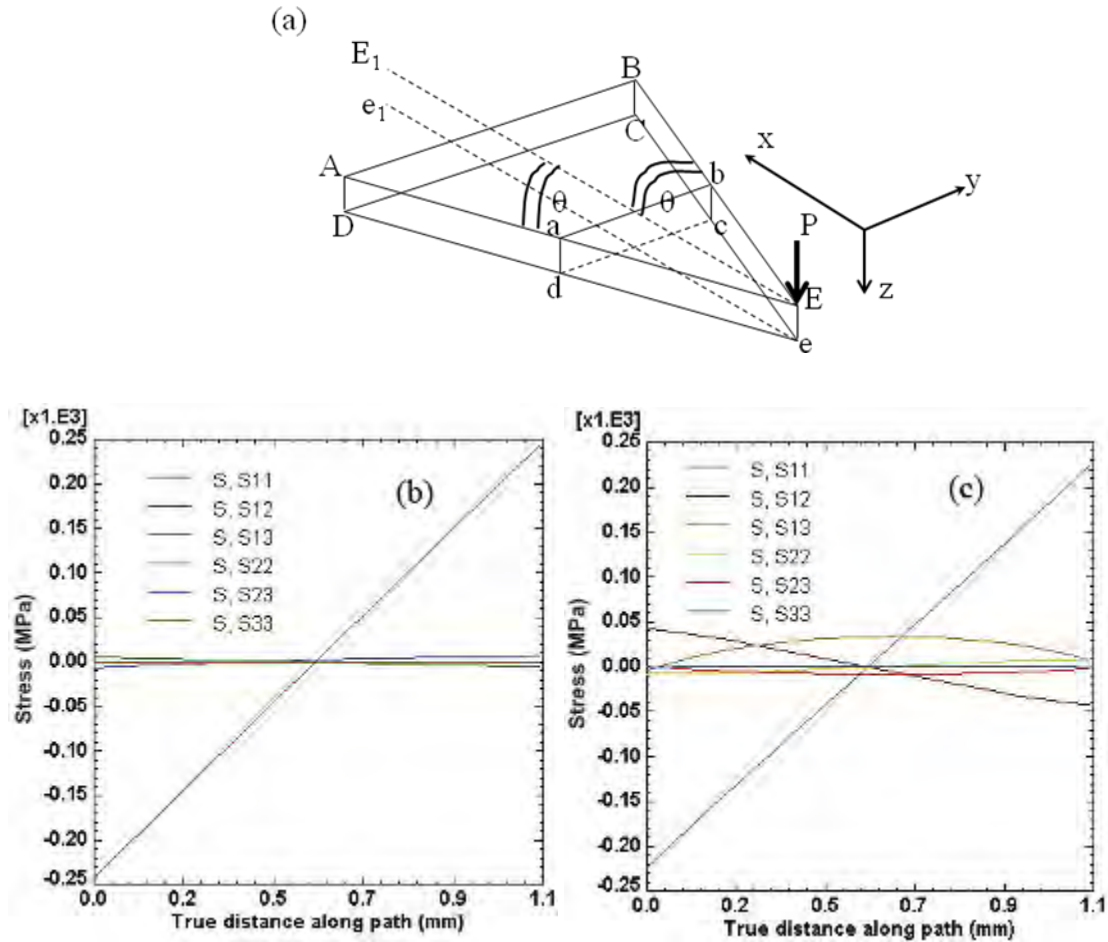

Fig. 1. (a) A schematic of the displacement controlled fatigue specimen shown as a cantilever with a typical rectangular cross-section (abcd) tapering from the fixed end ABCD to the pointed end Ee. The beam possesses bilateral symmetry along the plane EE_1e_1e. (b) Stress distribution along thickness (1.15 mm) near specimen centerline (i.e. EE_1/ee_1 in Figure 1a) at 25N bending force obtained by finite element simulation in ABAQUS (c) Stress distribution along thickness (1.15mm) towards specimen edge (i.e. ad/bc in Figure 1a) at 25N bending force obtained by finite element simulation in ABAQUS.

2.   EXPERIMENTAL DETAILS

The starting material was a 6.3 mm thick, rolled AA2098 alloy in T3 condition with base composition of Cu~3.5%, Mg~0.5%, Ag~0.4%, Li~1% and Zr~0.1% (hereafter called PA-T3). The original alloy plate aged at 160˚C for 19 hours (hereafter labeled PA-T8) and a friction stir welded (butt configuration) region (nugget portion only) of the PA-T3 alloy aged at 160˚C for 24 hours (henceforth referred as FSP-T5) were the two other microstructures used in this work. The three microstructures thus produced, were characterized using a combination of optical and orientation imaging microscopy (OIM). For OIM, samples were mechanically polished to a final polish of 0.02 μm and examined with a hot field emission gun scanning electron microscope (FEI Helios Nanolab) equipped with Nordylys camera and HKL technology. Precipitate distribution assessment was done using scanning transmission electron microscopy (STEM) on focused ion beam lift-out samples. All fractography experiments in this study were conducted using a Hitachi 4700S cold field emission gun scanning electron microscope operated at 15 kV. To evaluate the tensile and fatigue properties of the three microstructures, in-house designed subsize test beds were used [11, 15]. Parallel slices from the plate surface (within 1.5 mm from the top) and central region sectioned using a diamond saw were machined into subsize specimens using a computer numerically controlled milling machine. Similar subsize specimens were machined out from the nugget region of the friction stir welded plates (see Fig. 2). These subsize specimens were uniformly grinded and polished (1 μm finish) to 1 mm thickness for final testing.

3.   RESULTS

3.1   Grain size and precipitates

The microstructure of the parent alloy reveals a typical pancake shaped rolled structure with grains elongated in the rolling direction. The transverse grain dimensions were significantly smaller compared to the longitudinal. Figure 2(a) represents the typical parent alloy microstructure (PA-T3 / PA-T8) in a three dimensional perspective. Another feature of the parent microstructure was the presence of

occasional thick grains at regions near the surface (within one mm from plate surface). In Fig. 2(b) a typical OIM image of the friction stir nugget microstructure (FSP-T5) is shown. For the friction stir nugget sample (i.e. FSP-T5), grain size measurements were conducted at the mid-section of two different planes (A and B in Fig. 2(c)), one millimeter apart. No measurable grain size variation along this nugget depth was observed. In Table 1, a summary of grain size distribution for the three different microstructures as measured by linear intercept method is given.

To understand the nature of precipitates present, high angle annular dark field (HAADF) imaging of both PA-T3/PA-T8 microstructures were done (Fig. 3). The PA-T3 samples showed few circular precipitates. The PA-T8 microstructure on the other hand consisted of elongated needle shaped precipitates with incoherent equiaxed phases located at the grain boundaries. To ascertain the nature of precipitates, these micrographs were compared with an alloy of similar composition (Cu 3%, Li 1.6%, Mg.8%, Zr 0.2% and Al-balance) investigated by Crooks and Starke [16]. The PA-T3 structure in this work was analogous to the solutionized and naturally aged structure reported by Crooks and Starke [16]. The circular precipitates in PA-T3 microstructure were thus identified as the β' (Al_3Zr) phase. The δ' precipitates however remained unresolved. Identically, the observed T8 microstructure (Fig. 3(b)) compared well with the T8 condition of Crooks and Starke [16]. The needle shaped structures in Fig. 3(b) was therefore identified as the S' phase and the plate shaped precipitates as T_1 phase. The grain boundary phase observed in PA-T8 was probably a variant of the different T phases possible in Al-Li alloys [16].

Table 1 Grain size statistics for the three different microstructures of Al-Li used as measured by linear intercept method on OIM data.

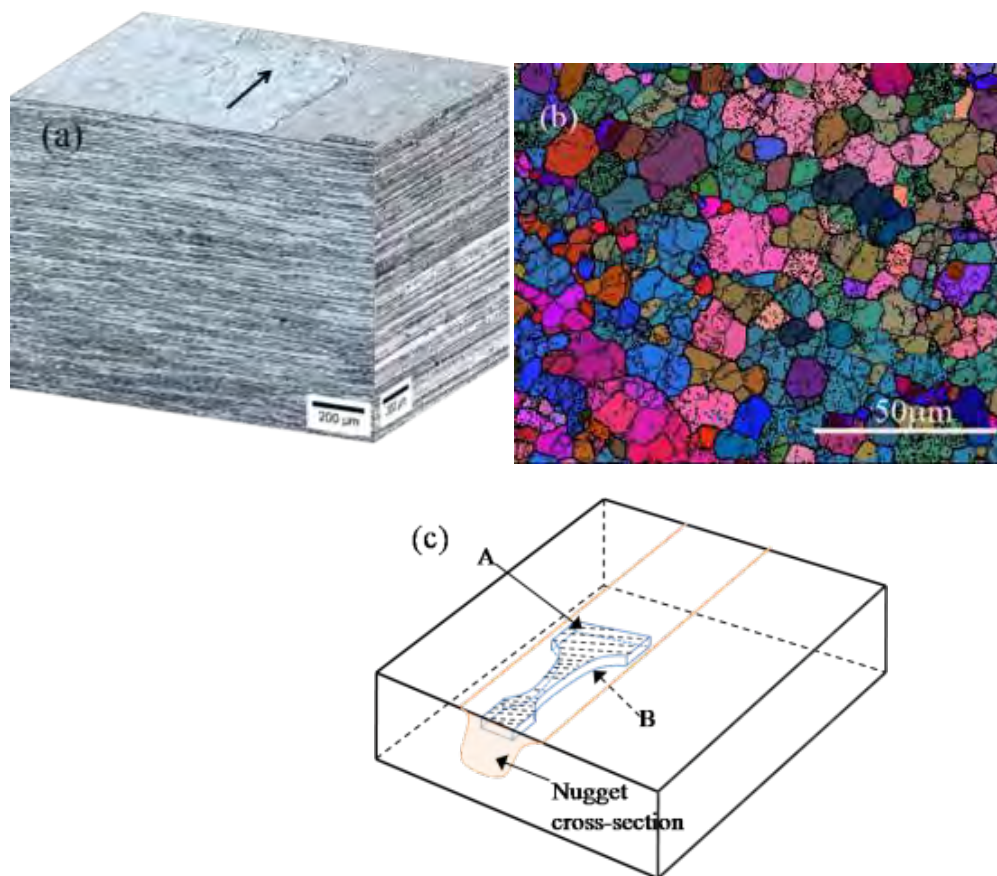| Microstructure	Average grain size (μm)	Minimum grain size (μm)	Maximum grain size (μm)
PA-T3/ PA-T8	5.8±1	1.4	34.4
FSP-T5	6.05±2.3	0.5	29

Fig. 2. (a) A three dimensional montage of the parent microstructure using optical microscopy; arrow shows the rolling direction. (b) Grain size distribution of the friction stirred microstructure as observed with orientation imaging microscopy using Euler angle coloring. Thick lines represents high angle grain boundaries (misorientation > 15˚) and the thin lines represents low angle grain boundaries (1˚< misorientation < 15˚). (c) Schematic illustration of friction stir processed zone, sampling plane positions A and B with respect to the weld surface.
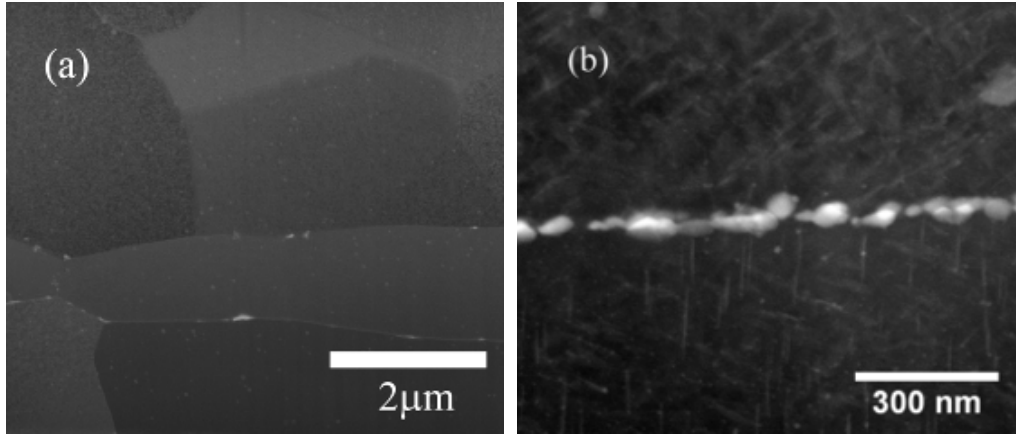
Fig. 3. HAADF-STEM images taken at 30 KV on FIB lift out samples. (a) PA-T3 microstructure showing

occasional small circular precipitates in the matrix along with sporadic precipitates at the grain

boundaries. (b) PA-T8 microstructure with irregularly shaped particles on the grain boundaries and

thin needle shaped precipitates located within the matrix.

3.2   Texture

The parent alloy (PA-T3/PA-T8) shows a strong rolling texture (Fig. 4), with the preferred

orientation being a combination of different texture components including $\{112\}\langle 111\rangle (\text{Copper} - \text{type})$,

$\{110\}\langle 112\rangle (\text{Brass} - \text{type})$ [17]. Thus, for both PA-T3 and PA-T8 microstructure a small fraction of the

$\{111\}$ poles were oriented at ~53° with the rolling direction (RD) while a higher fraction of the $\{111\}$

poles were oriented at ~19° with the RD (Fig. 4(a)). For the friction stir welded microstructure (FSP-T5) ,

texture data was obtained from a region parallel to the weld surface, the schematic position of which is

shown (plane 'A') in Fig. 2(c). The results confirm a shear texture, similar to that reported earlier [18,

19]. The data obtained from parallel planes at different heights (at 1.0 mm difference) exhibited a similar

pattern as shown in Fig. 4(b) indicating no change in texture within the friction stirred volume.
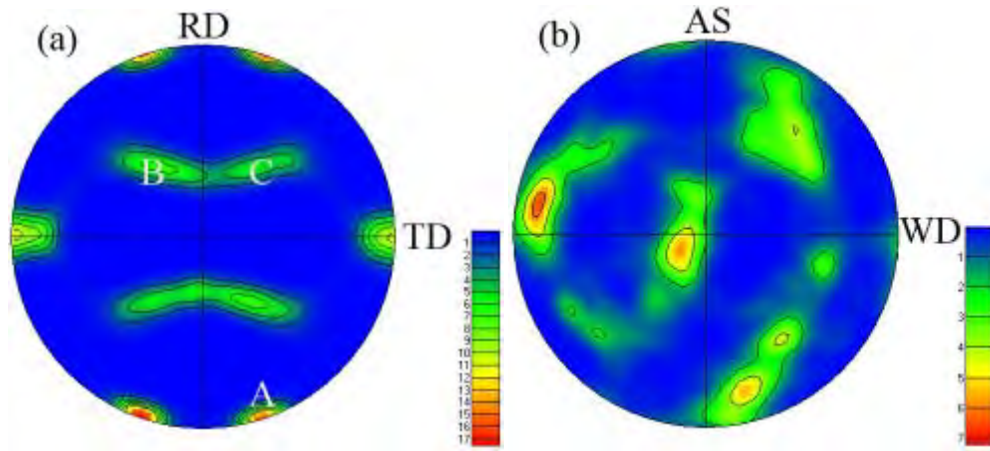
Fig. 4. (a) The 111 pole figure of the PA-T3/T8 microstructure, RD being the rolling direction and TD the transverse direction. (b) The 111 pole figure of FSP-T5, AS being the advancing side of tool and WD being the welding direction.

3.3   Tensile property

In Table 2 the strength and elongation values obtained from subsize tensile tests conducted on PA-T3, PA-T8 and FSP-T5 microstructures are summarized. No significant anisotropy in the tensile mechanical properties of FSP-T5 and PA-T8 microstructures was observed. However, for the PA-T3 microstructure a measurable directionality of strength and ductility was noted (Table 2). Another, remarkable feature of the PA-T3 microstructure was the absence of non-uniform elongation and necking for specimens oriented in the longitudinal direction (Fig. 5). This was unlike in PA-T3 samples of transverse orientation where a small, but definite non-uniform elongation was recorded (Fig. 5(a) and 5(c)). Further, for both PA-T8 and FSP-T5 microstructure, an extended non-uniform elongation zone was observed.

3.4   High cycle fatigue life

As mentioned in Section 3.1, a significant heterogeneity in the PA-T3 and PA-T8 microstructures (occasional large grains near the surface of the rolled sheets) was observed. To accurately estimate the fatigue property, the parent sheet specimens was therefore divided into two subcategories

depending on the depth of sample location from the plate surface. In the first subcategory, fatigue samples in transverse or longitudinal directions were machined from the center region where grains were finest and had the distribution given in Table 1 (abbreviated as PA-T3 and PA-T8, L/T, where L/T indicates longitudinal /transverse orientation). The second subcategory constituted of samples machined from the top one mm region of the plate surface (PAS-T3 and PAS-T8 L/T) where larger grains were observed. Additionally, to understand the effect of stress multi-axiality on fatigue life, samples of thickness 1.15-1.25 mm (from both PA-T3 and PA-T8 microstructures) were also tested (abbreviated as PA/PAS – T3/T8 – thick). In Fig. 2(c) the location of fatigue samples for FSP-T5 microstructure is shown. A summary of the variation in fatigue life for the different microstructures used in this study is shown in Fig. 6. The fatigue life variation for PA-T3 microstructure shows a level of scatter typically observed in commercial aluminum alloys. Thus, an order of magnitude difference in fatigue life was observed at low stress amplitudes, the scatter decreasing at higher stress levels (Fig. 6(a)). Perceptible difference in fatigue life with PA-T3 sample orientation was also noted.

Table 2 Summary of tensile test property of the different microstructures measured using subsize specimens [12].

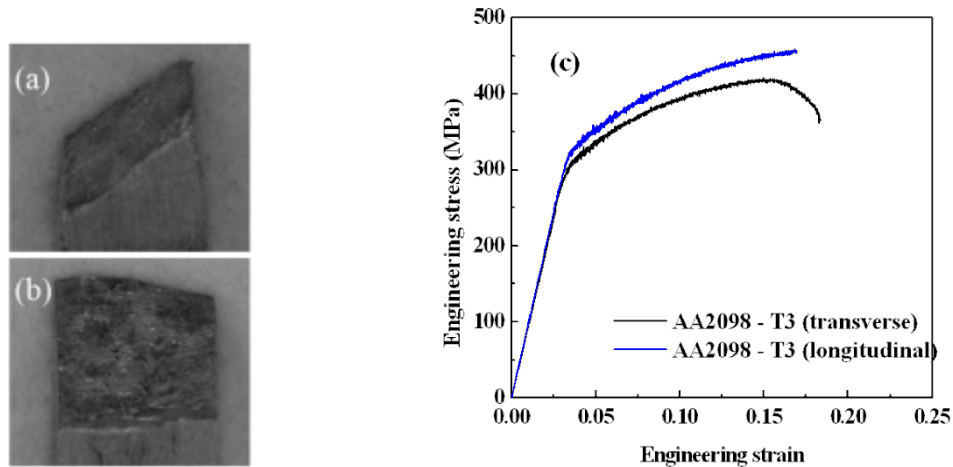| Microstructure	$\sigma_{YS}(MPa)$	$\sigma_{UTS}(MPa)$	$\varepsilon_u(\%)$	$\varepsilon_f(\%)$
PA-T3, longitudinal	327 ± 2	457 ± 2	12 ± 1	12 ± 1
PA-T3, transverse	294 ± 7	417 ± 1	12 ± 2	15 ± 1.4
PA-T8, longitudinal	540 ± 14	575 ± 17	7 ± 2	11 ± 0
PA-T8, transverse	528 ± 8	556 ± 7	7 ± 0.5	14 ± 2
FSP-T5, longitudinal	371 ± 5	443 ± 1.5	8 ± 1	18 ± 4
FSP-T5, transverse	382 ± 1.5	445 ± 1.4	9 ± 1	20 ± 0

Fig. 5 Fracture surface of 2098-T3 tensile specimen in (a) transverse orientation, and (b) longitudinal orientation. (c) The tensile stress strain curves of 2098-T3 specimens in transverse and longitudinal orientations.

Thus, PA-T3 (T) samples showed a better fatigue life compared to PA-T3 (L) samples irrespective of the sample thickness tested. However, for PAS-T3 (T) samples a reduction in fatigue life at low stresses was observed. Compared to PA-T3 microstructure the overall scatter in fatigue life for PA-T8 microstructure was higher. The life varied approximately half an order of magnitude at high stresses to almost two orders at lower stress levels (Fig. 6(b)). Thus, PA-T8 (L) samples showed a better fatigue life irrespective of the sample thickness, while PA-T8 thick (T) samples showed a poor fatigue life. A maximum decrease in the fatigue life was observed for PAS-T8 (L), PAS-T8 thick (T) and PA-T8 thick (T) samples. Due to such high fatigue life scatter, a more effective representation of the S-N curve for PA-T8 microstructure can be given in terms of the two separate S-N curves as shown in Fig. 6(c). Thus, although the median fatigue life for PA-T8 microstructure was high, the overall fatigue performance of PA-T8 was comparable to that of PA-T3 and FSP-T5 microstructures.

Approved for public release; distribution unlimited.
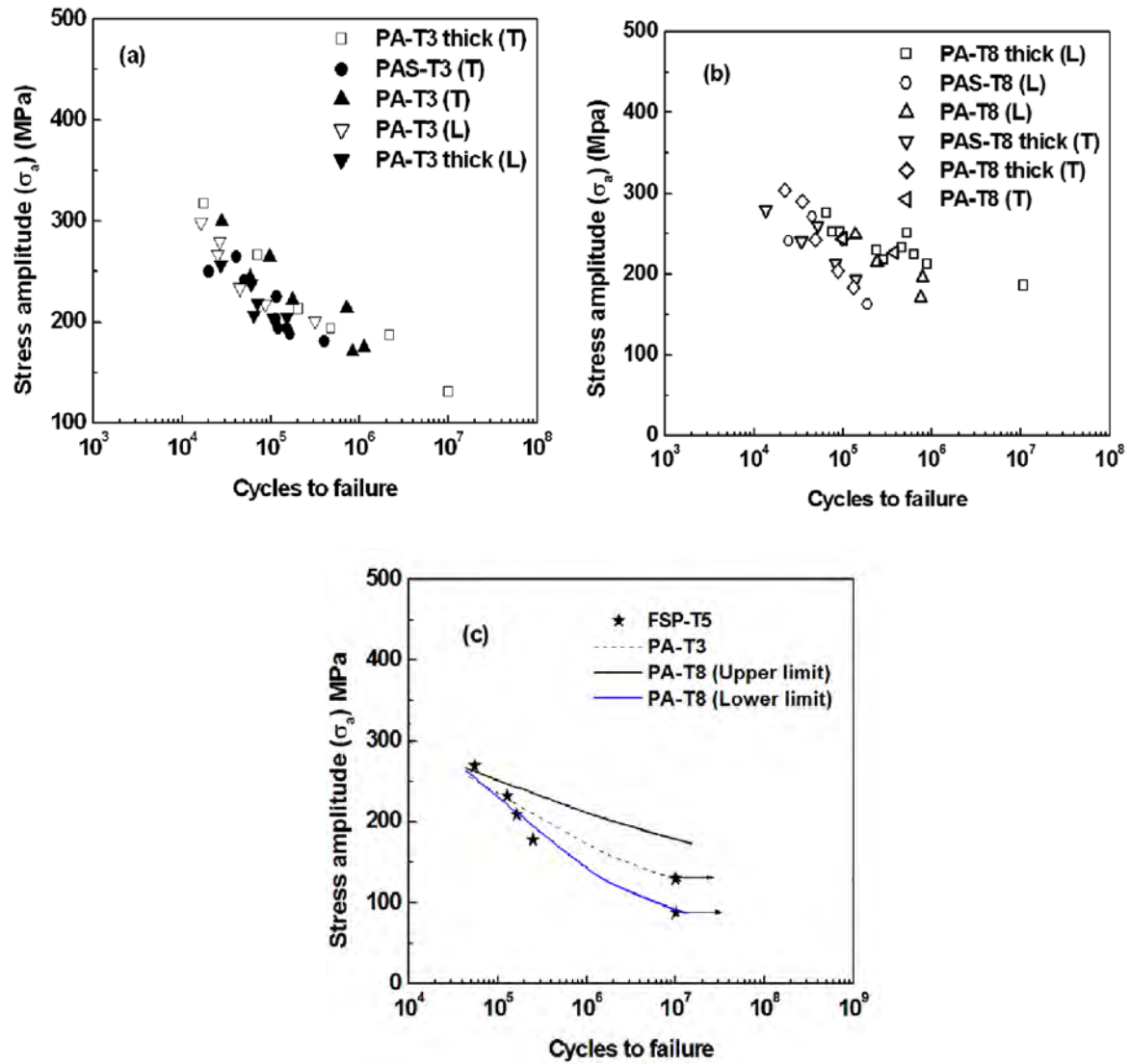
Figure 6. S-N curve of Al-Li alloy for different orientations (a) samples PA-T3 L/T, PAS-T3 (T) and PA-T3 thick (L/T), (b) samples PA-T8 thick (L/T), PA-T8 (L), PAS-T8 (L) and PAS-T8 thick (T), and (c) samples from FSP-T5 in the weld direction with overall S-N curves for PA-T3, PA-T8 and the upper and lower limit curves for PA-T8 superimposed.

3.2   Fracture surface morphology

The fracture surface morphology (Fig. 7) of the three different microstructures used in this study exhibits the characteristic three stage crack propagation typical of face centered cubic metals [20].

However, subtle differences between the three different microstructures at each individual stage were visible. Consider the PA-T3 type of specimens first. The stage-I crack propagation of PA-T3 (L) samples was distinguished by extended inclined smooth fracture surfaces (Fig. 7(a)) oriented at an angle of $30 \pm 2\degree$ with the direction of rolling (Fig. 7(e)). The fracture in PA-T3 (T) samples were however different, with the inclined smooth surface typical of PA-T3 (L) samples limited to a much smaller zone (Fig. 7(b)). The fracture surface corresponding to stage-I crack propagation in PA-T8 specimens on the other hand showed a crystallographic type of crack propagation with prominent ridges and plateaus (Fig. 7(c)). In some instances tire tracks pointing in the crack propagation direction were also observed (Fig. 7(f)). The stage-I crack propagation zone of FSP-T5 samples appeared different from both the PA-T3 and PA-T8 samples (compare Fig. 7(c) and 7d). The nature of crack propagation was more tortuous compared to the faceted structures appearing in the PA-T3/PA-T8 samples.

Another important aspect observed during fatigue fracture was the tendency towards extended de-lamination in both PA-T3 and PA-T8 microstructures (Fig. 8). The de-lamination cracks were oriented in a direction complementary to the loading axis. In all cases, these de-laminations occurred along the boundary of two fracture surface facets indicating a typical intergranular type of failure. Although such extended de-lamination cracking was not observed in the FSP-T5 specimens, small cracks in between the fracture facets were visible particularly in the stage-I region. An additional feature observed in PA-T8 samples, was the interlinking of de-lamination cracks at regions midway between surface and center of fatigue specimens (Fig. 8(b)). This feature was particularly noted in PAS-T8 thick (T), PA-T8 thick (T) and PAS-T8 (L) samples and was accompanied by a maximum reduction in fatigue life.
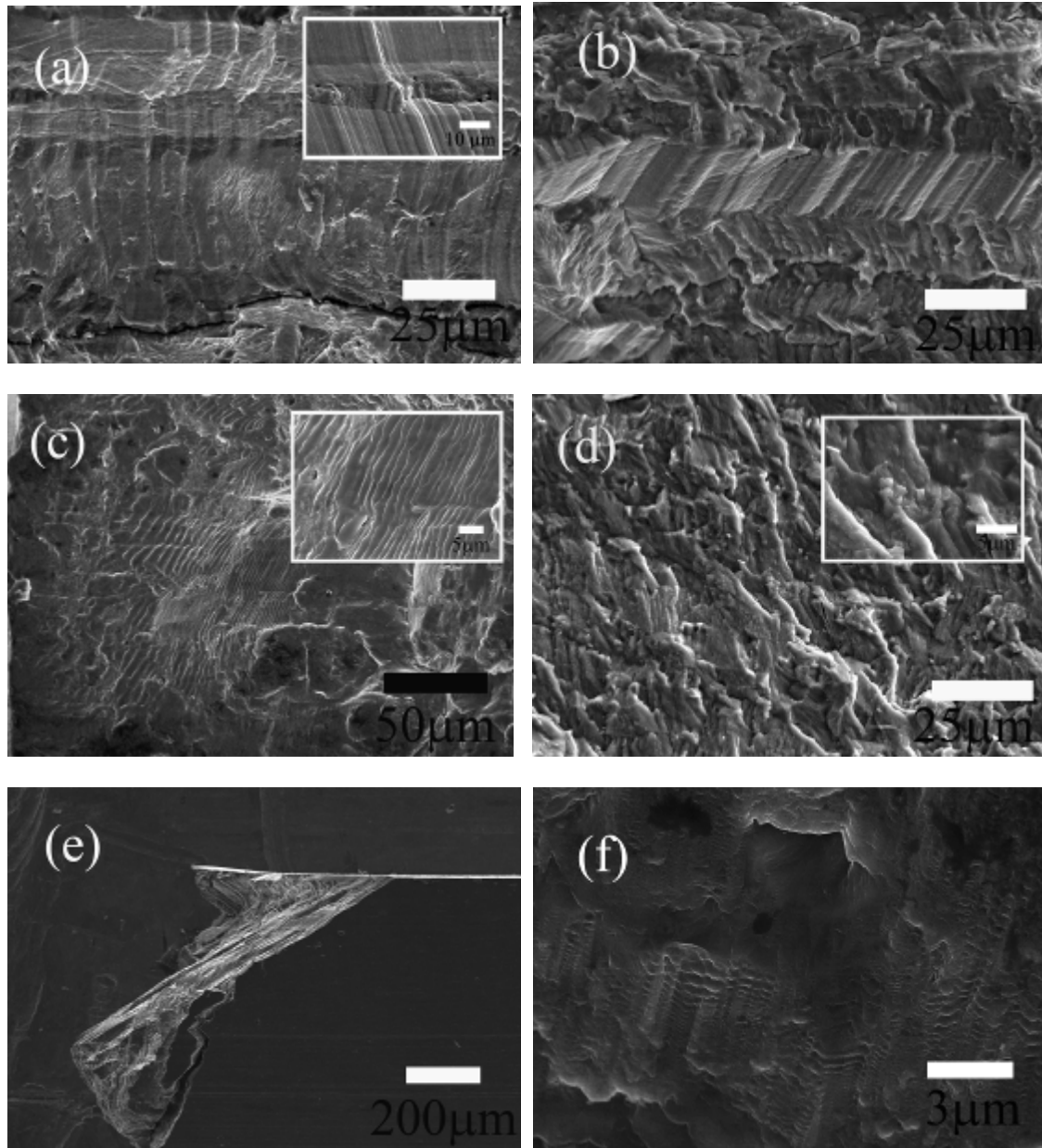
Fig. 7. Typical stage – I crack propagation characteristics for various specimens: (a) PA-T3 in

longitudinal with inset showing the details. (b) PA-T3 in transverse direction. (c) PA-T8

longitudinal / transverse with inset showing regular shape ridge like features in details. (d) FSP-T5

in weld direction with irregular ridges formed. (e) The inclined stage –I crack propagation in PA-

T3 samples oriented in longitudinal direction. (f) Tire tracks in a PA-T8 sample.

The stage-II crack propagation region in PA-T3 (L/T) samples showed coarse striation marks accompanied by extensive tears along crack propagation plane (Fig. 9). For PA-T8 specimens, the striation spacing however varied between both fine and coarse (compare Fig. 9(c) and 9d). Additionally, the extent of tearing on crack propagation plane for PA-T8 microstructure was significantly lower compared to the PA-T3 microstructure (compare Fig. 9a to 9d). In FSP-T5 specimens, the striations appeared to be more restricted and localized in nature (Fig. 9e) with reduced crack plane tearing. The stage-III crack propagation zone in all microstructures, were similar in nature and were typical of failure by void growth.
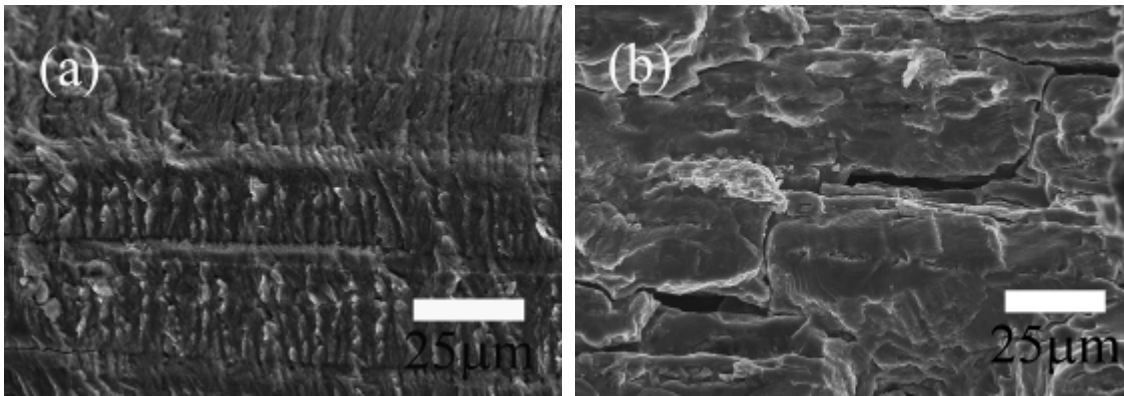

Fig. 8. De-lamination and the effect of stress amplitude on (a) PA-T3 microstructure in transverse direction at 170 MPa showing de-laminated region between the regularly spaced fracture surface facets. (b) PA-T8 (thick) microstructure in transverse direction at 209 MPa showing de-laminated regions which have joined together to form extended intergranular type of cracking.
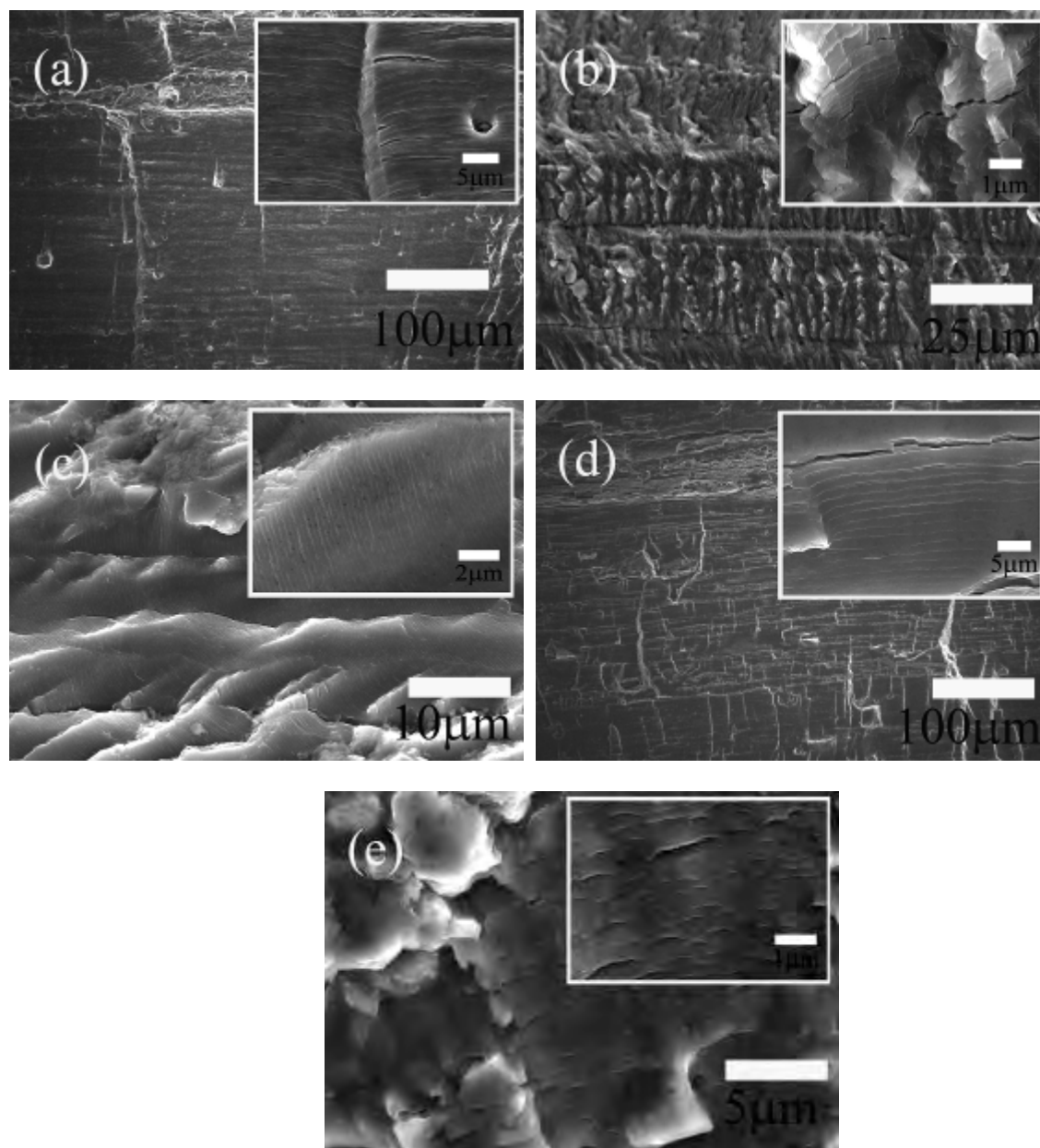
Fig. 9. Stage-II crack propagation in (a) PA-T3 sample in the longitudinal direction. (b) PA-T3 sample in the transverse direction. (c) PA-T8 sample in the transverse direction. (d) PA-T8 sample in longitudinal direction. (e) FSP-T5 sample.

4. DISCUSSION

As already noted, the fatigue property of PA-T8 microstructure shows a wider scatter compared to PA-T3 samples. The FSP-T5 samples on the other hand show a mean fatigue life which is similar to the PA-T3 microstructure. Significant differences in the microstructure and fracture surface appearance were also noted. In the following sections the effect of microstructure and stress states on the fatigue life has been discussed in more details.

4.1 Fatigue crack propagation and nature of slip

As already discussed in Section 3.3, the PA-T3 tensile specimens oriented in longitudinal direction exhibited no non-uniform elongation. This was unlike the transverse orientation samples where a small but definite non-uniform elongation was observed. Non-uniform elongation in tensile specimens is associated with a tri-axial state of stress with slip occuring on multiple crystallographic planes [21]. Therefore, the lack of non-uniform elongation in longitudinal PA-T3 samples signifies a localization of dislocation movement in specific slip systems.

In fact, such localization of slip occurred even in PA-T3 (L) fatigue samples in the crystallographic crack propagation regime. The smooth (Fig. 7(a)), inclined (Fig. 7(e)) crack propagation in PA-T3 (L) samples compared to the random crack propagation in PA-T3 (T) samples (Fig. 7(b)) illustrates this differences in slip. To understand the issue further, the interaction between PA-T3/PA-T8 texture, precipitate and loading direction needs detailed consideration.

Considering {111}<110> as the active slip system, tensile forces acting along a given direction will cause shear stresses on the (111) plane. The magnitude of this shear stress is determined by its corresponding Schmid factor. For parent microstructure specimens with loading axis aligned in rolling direction, this Schmid factor value varied between 0.395-0.425 (Fig. 10). In contrast, for specimens in transverse orientation the Schmid factor value showed a uniform distribution varying between 0.285-0.45 (Fig. 10). The high Schmid factor value combined with continuous reduction in critical resolved shear

stress (CRSS) of (111) planes due to shearing of coherent ordered δ' precipitates is expected to cause planar slip movement in PA-T3 (L) samples [6].

Consequently, crack propagation in PA-T3 (L) samples was expected to progress along (111) planes oriented at an angle of ~20° with the rolling direction (Fig. 7(e)). This crack plane inclination deviates by ~10° from the expected inclination for the (111) plane corresponding to pole position A (Fig. 4(a)). Such deviation (~3 to 10°) from the close packed slip plane has previously been reported in the crystallographic studies on fracture surface facets for specimens in L-T orientation for Al-Cu-Li alloys with δ' precipitates [22]. On the other hand, the low Schmid factor values in PA-T3(T) specimens were expected to reduce the shearing of δ' phase substantially. Consequently, other {111}<110> slip systems get activated resulting in a random stage-I crack propagation. An important point is that, despite having a texture similar to the PA-T3 microstructure, fatigue crack propagation in both PA-T8 (L/T) specimens remained random and homogeneous. This clearly indicates that precipitate nature (non-shearable) plays a key role in determining the crack propagation characteristics of the investigated Al-Li alloy [6]. The needle shaped S' phase present in PA-T8 specimens will promote a more uniform slip dispersion among the {111}<110> slip systems. Consequently PA-T8 (L/T) specimens exhibits, a random crack propagation irrespective of their orientation.

The wavy stage-I fracture surface characteristics of FSP-T5 samples can be ascribed to the effect of grain aspect ratio and precipitates present. The smaller effective grain size of FSP-T5 (Table 1) increases the nucleation stress required to generate dislocations from grain boundaries compared to the coarser parent microstructure [23]. The increased nucleation stress combined with resistance to slip due to precipitates present (similar to that of PA-T8) restricts the overall dislocation movement in FSP-T5 specimens. Consequently, a more tortuous crack movement in the stage-I regime was observed. Reverting back to the stage-II crack propagation characteristics; an increased incidence of tearing on striation planes of PA-T3 (Fig. 9(a) and 9(b)) samples compared to both PA-T8 and FSP-T5 was observed. Considering the alternating slip model for stage-II crack growth [24], such crack plane tearing indicates a stress concentration on close packed slip planes. For PA-T3 (L/T) samples the ordered precipitates (δ') present

Approved for public release; distribution unlimited.

will resist the to and fro dislocation movement equally during stress reversals. In the case of PA-T8/FSP-T5 samples the situation is however different. For both microstructures, S' the principal hardening phase strengthens the matrix by dislocation interaction with the stress fields [25]. Any dislocation movement across the particles (e.g. during tension cycle) destroys this stress field. Consequently, reverse dislocation movement (compressive cycle) becomes easier (Bauschinger effect) [20, 25]. Thus, localized stress concentration in PA-T3 samples is easier compared to the PA-T8/PA-T3 microstructure. The detailed fracture surface analysis presented above therefore indicates a close relationship between texture and precipitate nature on stage-I/II crack propagation. In the next section, the effect of crack propagation on fatigue life for the three different microstructures and their interaction with grain size is discussed in more detail.
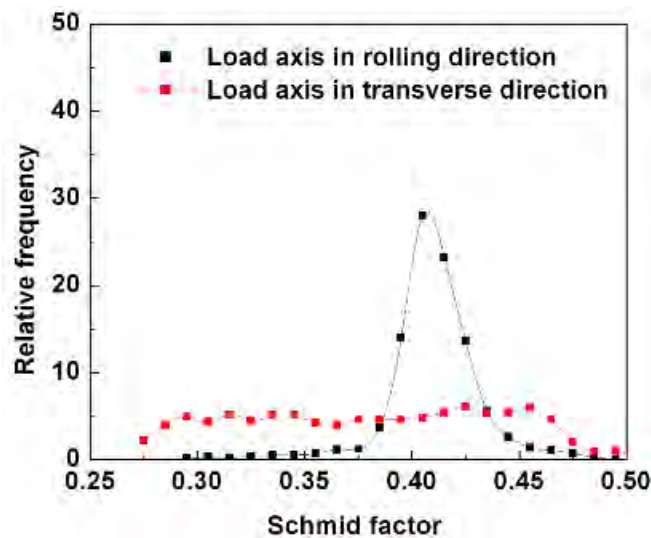

Fig. 10. The Schmid factor distribution for {111}<110> slip in PA-T3/PA-T8 specimen with load axis oriented in rolling/transverse direction. The results are from an OIM data acquired over an area of $660*525\ \mu m^2$.

4.2 Fatigue life: crack propagation and grain size effect

As already discussed in Section 3.4, fatigue life of PA-T3 samples oriented in longitudinal direction showed a reduced fatigue life compared to the transverse irrespective of sample thickness tested.

To understand the reason behind this decrease, the nature of stage-I fatigue crack propagation for PA-T3 samples is now considered. As already indicated fatigue crack propagation in PA-T3 (L) samples was influenced by texture/precipitate and occurred along definite crystallographic plane. On the other hand, the PA-T3 (T) samples showed a rough fracture surface indicating crack propagation along multiple slip planes. The limited crack deflection and crack face asperities in PA-T3 (L) samples (compared to PA-T3 (T)) lead to a decreased roughness induced crack closure [20]. Consequently, a reduction in stage-I fatigue life for PA-T3 (L) samples was expected. The slight reduction in fatigue life for PAS-T3 (T) samples can be correlated to the effect of grain boundaries on the rate of crack growth. In high cycle fatigue, grain boundaries are known to act as a barrier to crack propagation particularly at the initial stages of crack propagation [20]. This retardation in crack growth rate results in improved fatigue endurance which is given as [26],

$$\sigma_{th} = \sigma_{fr}^* + \frac{K_c^m}{\sqrt{(\pi/2)d_g}}$$ (4)

where σ_{fr}^* is the friction stress for dislocation movement, K_c^m is the microscopic stress intensity factor and d_g is the grain size. Thus, for larger grained PAS-T3 (T) samples, the rate of crack propagation (Stage-I) will be higher compared to PA-T3 (T) specimens of smaller grain size as the sheet surface consisted of occasional large grains, almost half an order of magnitude higher than the average grain size. Although the specific processing details of the Al-Li alloy used in this study are unknown, the microstructure clearly indicates the occurrence of abnormal grain growth near the surface. Abnormal grain growth is generally known to occur in metals where normal grain growth is suppressed [17, 27]. Considering the presence of Al_3Zr particles (to prevent grain growth/ recrystallization) abnormal grain growth can therefore be a matter of concern for the Al-Li alloy studied.

Unlike PA-T3, for PA-T8 samples fatigue life was highest for both PA-T8 (T)/PA-T8 (L) specimens irrespective of the sample orientation. In fact, considering the similar slip and stress-strain characteristics of PA-T8 samples (Table 2) a change in fatigue life with orientation was not expected. The

Approved for public release; distribution unlimited.

improved fatigue life was therefore associated with an increase in crack deflection and fracture surface asperities due to the nature of precipitates present. On the other hand, a significant decrease in fatigue life was observed for PA-T8 thick (T) compared to PA-T8 thick (L) specimens for stresses below ~250 MPa. The extensive intergranular cracking observed in PA-T3 thick (T) samples (Figure 8b) indicates that grain boundary weakness contributed to this decrease in fatigue life. Another interesting feature was the similarity in fatigue life for PAS-T8 (L) and PAS-T8 thick (T) specimens with PA-T8 thick (T) samples. The inherently weaker grain boundary of PA-T8 microstructure catalyzed by other microstructural features was therefore suspected to be a principal reason behind this fatigue life decrease. In the next section this broader role of microstructure and de-lamination effect on the HCF life of Al-Li alloys is discussed in more details.

4.3   De-lamination tendency

As already mentioned, in both PA-T8 and PA-T3 microstructures (Fig. 8a and 8b) a de-lamination tendency was observed, the severity being more apparent in PA-T8 microstructure. These de-laminations occurring at the grain boundary regions resulted in an intergranular type of cracking for PAS-T8 and PA-T8 thick (T) samples. To understand this issue further, the interaction between stresses in a displacement controlled bending fatigue test and microstructural features needs further consideration. As noted earlier, the PA-T8 microstructure consisted of extensive grain boundary precipitates which were incoherent in nature. These incoherent precipitates act as regions of discontinuity causing triaxial stress distribution in the bending fatigue specimen. Under the application of bending stress these discontinuities at the grain boundary regions create de-laminations within the specimen (Fig. 9 b - c). In other words, the continuum structure of specimen yields to a more discontinuous laminated structure. Again, depending on the grain orientation (i.e. specimen orientation) the nature of de-lamination cracks inside the specimen changes. Thus, for specimens in longitudinal orientation, the discontinuities are approximately in crack divider orientation while for transverse orientation it is more of the short transverse type. This is chiefly due to the elongated grain shape in the present alloy where transverse dimensions were much smaller than

the longitudinal orientation. Consequently, for PA-T8 (L) specimens intergranular crack propagation is expected to be difficult, while the reverse will be true for PA-T8 (T) specimens. Thus, although PA-T8 (L) specimen (irrespective of sample thickness) shows better fatigue life, the same is not true for PA-T8 thick (T) specimens. An alternative explanation can be given in terms of stress concentration differences between transverse and longitudinal specimens. Assuming a continuous grain boundary precipitate, grains in AA2098-T8 can be approximated as elliptical holes whose depth equals the grain size (Table 1). The dimension of ellipse approximated as equal to the longitudinal and transverse dimension of a grain with major axis length ~250 µm and minor axis ~100 µm. For simplicity, consider a uniform rectangular solid (Fig. 11(a)) whose boundary conditions are chosen such that the resultant stresses on surface of interest (i.e. A_1) is similar to that inside the bending fatigue specimen. In Figs. 11(b)-(c), the forces applied and the corresponding stresses generated at the sample center along X (Path: 1) and Y (Path: 2) directions are shown. It can be seen that the stresses generated were similar to that predicted at the tension side of a 1.15 mm thick bending fatigue sample subjected to 25N load (Fig. 1(b)). The simulated stress state in a PA-T8 (T) specimen with an elliptical hole inserted on face A_1 is shown in Fig. 12(a). The stresses generated around the elliptical hole along Path-1 and Path-2 (Fig. 12(a)), on application of forces similar to Figure 11a, are shown in Fig. 12(b) and 12(c). The results show, that elliptical holes in transverse orientation, creates a s_{11} stress concentration which is 1.6 times higher than that in Fig. 11(b) - (c). The corresponding stress distribution in a PA-T8 specimen with longitudinal orientation is shown in Fig. 13(b) and 13(c). As may be noted, a significant difference in the stress concentration distribution exists between transverse and longitudinal specimens. Thus, for PA-T8 (T) specimens a stress concentration is noticed at both the sharper (Point A in Fig. 12(a)) and flatter perimeters (Point B in Fig. 11(a)) of the ellipse. On the other hand, for PA-T8 (L) specimens the stress concentration is observed at the sharper surface (Point B in Fig. 12(a)) only. This added stress-concentration in PA-T8 (T) specimens compared to PA-T8 (L) is expected to favor intergranular cracking with resultant fatigue life reduction. Additionally, the favorable Schmid factor in transverse orientation specimens favors slip deformation as already discussed in section 3.3.
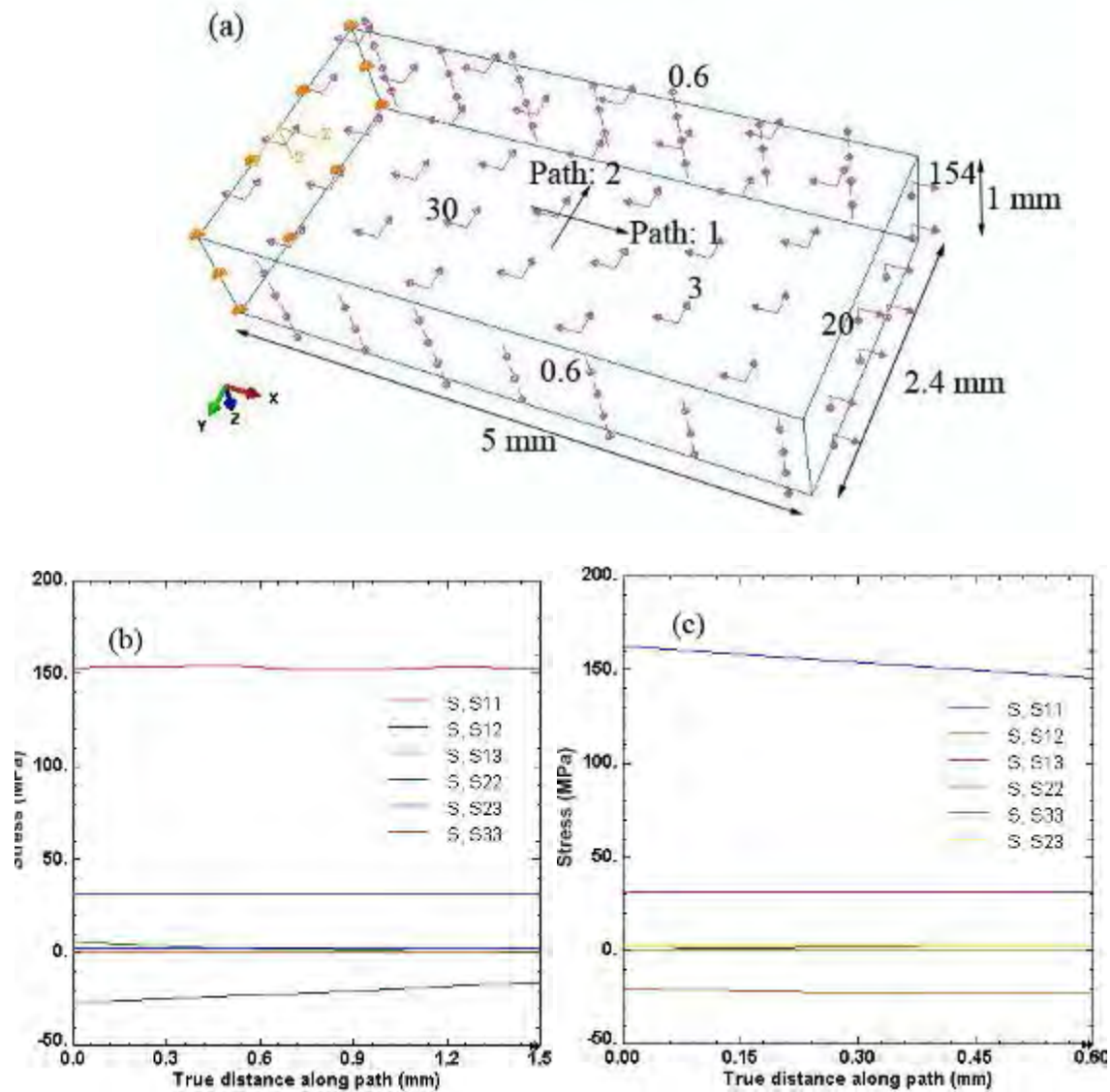
Fig. 11. (a)The forces applied on a rectangular cross-section simulating the stresses generated in the bending fatigue samples on the top surface. The in-plane arrows indicate shear forces while out of plane arrows indicate axial forces. The dimension of the solid section shown are in mm's. The numbers by the side of each arrow indicates the magnitude of force applied in Newtons. (b) The overall stress distribution along Path: 1 shown in Figure 11a. (c) The overall stress distribution along Path: 2 shown in Figure 11a.
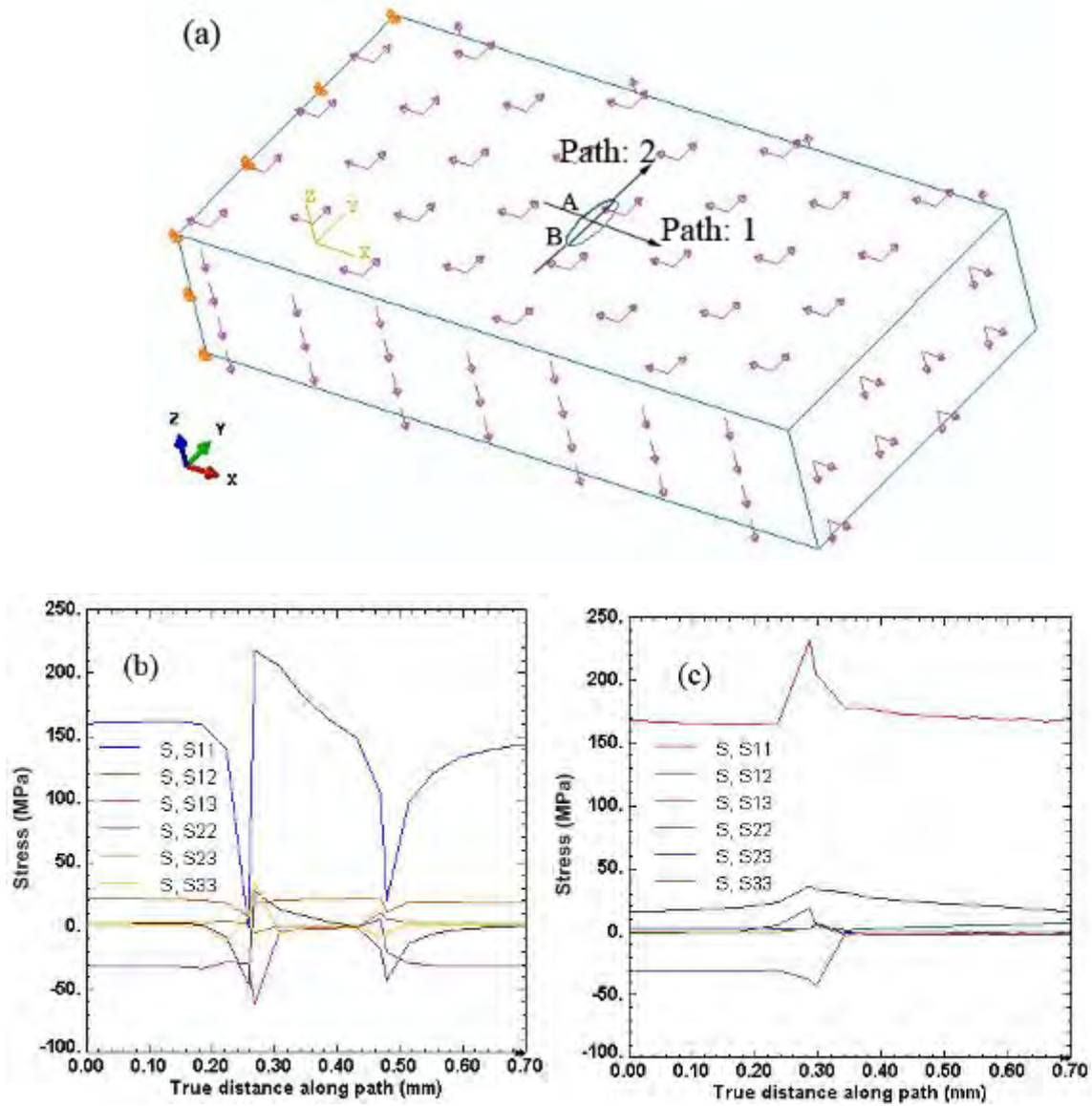
Fig. 12. (a) Simulation condition for PA-T8 bending fatigue specimen in transverse orientation. The forces applied are same as in Figure 11a. (b) The stresses generated along Path:1 in Figure 12a. (c) The stresses generated along Path: 2 in Figure 12a. Note, the stress concentration points generated compared to Figure 11b and 11c.
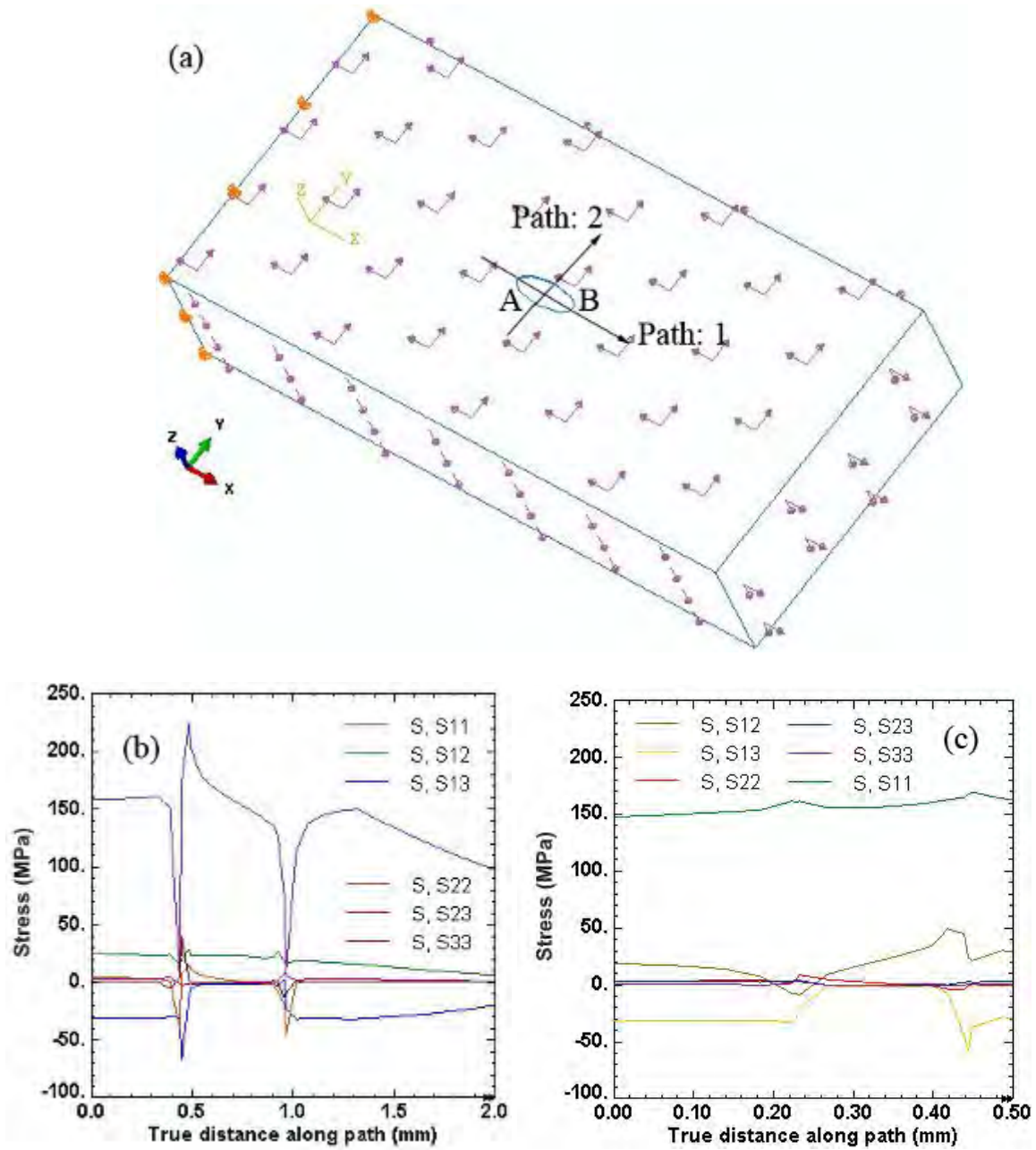
Fig. 13. (a) Simulation condition for PA-T8 bending fatigue specimen in longitudinal orientation. The forces applied are same as in Figure 11a. (b) The stresses generated along Path:1 in Figure 13a. (c) The stresses generated along Path: 2 in Figure 13a. Note, the stress concentration points generated compared to Figure 11b and 11c.

Here, it is important to note that although the fatigue life of PA-T8-thick (T) specimens were lowered, fatigue life of PA-T8 (T) specimens were comparable to PA-T8 (L) samples. This discrepancy can be explained on the basis of de-lamination which reduces the effective thickness of fatigue samples at a localized level. Thus for a given initial stress amplitude (fixed *w*) this in effect increases the local axial stress generated in de-laminated layers (Eq. 3). Again, at a given stress level '*w*' is smaller for lower sample thickness. Considering de-lamination thickness to be independent of sample dimensions, an increase in sample thickness (increased '*w*') would therefore result in higher localized stresses on de-laminated layers for a given stress amplitude. Previously, for Al-Li alloys only samples in S-L and S-T orientations were expected to have poor crack propagation resistance due to de-lamination [9]. However, for the multiaxial bending fatigue conditions used in this work, even T-S orientation exhibits poor crack propagation resistance depending on specimen thickness tested. Thus, under the multiaxial bending fatigue conditions sample thickness will play a significant role in controlling fatigue life.

5.   CONCLUSION

1. A rolled Al-Li-Cu-Mg-Zr-Ag system with Cu:Li ratio greater than 2.5 was studied. In T3 condition, tensile stresses in rolling direction causes planar slip. The effect being initiated by the presence of ordered coherent δ' phase coupled with a favorable rolling texture. This results in stage-I propagation where the fracture surface is parallel to the {111} planes.

2. For T3 alloy stressed in transverse direction the effect of planar slip on fracture surface orientation was nominal. Similarly, no effect of texture on crack propagation was observed for the T8 alloy. This has been ascribed to the slip dispersion caused by the needle shaped S phase precipitates accompanied with a Schmid factor effect. The FSP-T5 microstructure had a shear texture but do not show any texture effect on stage-I crack propagation

3. An effect of grain size on the high cycle fatigue life for both T3andT8 microstructure was observed. For T3 condition, at stresses below 200 MPa, samples from sheet surface containing large grains

showed lower life. For T8 condition, the effect was observed up to 250 MPa. Above these stress limits, both T3 and T8 microstructure show limited effect of grain size on fatigue life. For samples from internal regions of the sheets the fatigue life was consistently high compared to the surface samples. The effect has been ascribed to the effect of grain size on crack propagation in stage -I. The FSP-T5 microstructure shows a fatigue life similar to that of the T3 heat treated condition.

4. A tendency for de-lamination was observed in both T3 and T8 conditions. The de-lamination led to intergranular type of fracture under multi-axial conditions. The effect was particularly noticeable in T8 samples. This has been attributed to the presence of grain-boundary second phase of Al-Cu-Li type, causing grains to behave as stress raisers. The fatigue life reduction in both T3 and T8 surface samples is accentuated by this de-lamination tendency. Similarly, the transverse T8 samples showed lower fatigue life compared to longitudinal specimens. However, thinner transverse T8 samples (~1 mm) showed no effect on fatigue life. This was due to the nature of multiaxial stresses created during bending fatigue.

REFERENCES

[1]   N.A.Belov, D.G. Eskin, A.A. Aksenov. Multicomponent Phase Diagrams: Applications For Commercial Aluminum Alloys, First ed., Elsevier, 2005.

[2]   T.H.Sanders, E.A.Starke. Overview Of The Physical Metallurgy In The Al-Li-X Systems in: E.A. Starke, Jr., T.H. Sanders, Jr (Eds.). Proceedings of the Second International Aluminum-Lithium Conference sponsored by the Nonferrous Metals Committee of The Metallurgical Society of AIME at Monterey, California, April12-14, 1983.

[3]   K.S.Kumar, S.A. Brown and J.R.Pickens, Acta Mater.1996;44:1899.

[4]   M. Tiryakioglu and J T.Staley. Physical Metallurgy and the Effect of Alloying Additions in Aluminum Alloys, in: G.E. Totten and D. ScottMckenzie (Eds.). Handbook in Aluminum Vol.1, Physical metallurgy and Processes, New York, Marcel Dekker Inc. 2003.

[5]   U.F. Kocks, H.Mecking, Prog. Mater. Sci. 2003;48:171.

[6]   V.Gerold and H.P. Karnthaler, Acta Metall. 1989;37:2177.

[7]   T.H. Sanders Jr and E.A. Starke Jr, Acta Metall. 1982;30:927.

[8]   S. Suresh, A.K. Vasudevan, M. Tosten and P.R. Howell, Acta Metall. 1987;35:25.

[9]   K.T. Venkateswara Rao and R.O. Ritchie, Inter. Mater. Rev. 1992;37:153.

[10] D.Khireddine, R. Rahouadj and M. Clavel, Acta Metall., 1989;37:191.

[11] P.S.De, C.M. Obermark, R.S. Mishra, J. Test Eval. 2008;36(4):JTE101669.

[12] S. Timoshenko, D.H. Young. Elements of strength of materials, Fifth ed., D. Van Nostrand Co.,
     1968.

[13] J.D. Embury, N.J. Petch, A.E. Wraith, E.S. Wright, Trans. AIME 1967;239:114.

[14] R.W. Hertzberg. Deformation and Fracture Mechanics of Engineering Materials, John Wiley &
     Sons, 1976.

[15] R.S. Mishra, S.R. Sharma, M.A. Mara, M.W. Mahoney: ASM International Joining of Advanced and
     Specialty Materials III, M. Singh et al Eds.,2000:157.

[16] R.E. Crooks and E.A. Starke Jr, Metall. Trans. A 1984;15:1367.

[17] F.J.Humphreys andM.Hatherly. Recrystallization and related annealing phenomenon, First ed.,
     Elsevier, 1995.

[18] D.P. Field, T.W. Nelson, Y. Hovanski and K.V.Jata, Metall. Mater. Trans. A, 2001;32A:2869.

[19] G.R. Canova, U.F. Kocks and J.J. Jonas, Acta Metall. 1984;32:211.

[20] S.Suresh. Fatigue of materials, Second ed., Cambridge University Press, 1998.

[21] R.W. Hertzberg. Deformation and fracture mechanics of engineering materials, Fourth ed., John
     Wiley and Sons, 1996.

[22] Y.Ro, S.R. Agnew & R.P. Gangloff, Metall. Mater. Trans. A, 2007;38A:3042.

[23] J.P. Hirth, J. Lothe. Theory of dislocations, McGraw - Hill Inc, 1968.

[24] P. Neumann, Acta Metall. 1969;17:1219.

[25] R.E. Stoltz, R.M.N. Pelloux, Metall. Trans. 1976;7A:1925.

[26] K. Tanaka, Y. Nakai, M. Yamashita, Inter. J. Frac. 1981;17:519.

[27] F.J. Humphreys, Acta Mater.1997;45:5031.